Synthesis and magnetocaloric characterization of
rapidly solidified ErMn$_2$ melt-spun ribbons

J.L. Sánchez Llamazares [a,*], P. Ibarra-Gaytán [a], C.F. Sánchez-Valdés [b],

P. Álvarez-Alonso [c], A.D. Martínez-Iniesta [d]

[a] *Instituto Potosino de Investigación Científica y Tecnológica A.C., Camino a la Presa San José 2055, Col. Lomas 4ª, 78216 San Luis Potosí, S.L.P., México.*
[b] *División Multidisciplinaria, Ciudad Universitaria, Universidad Autónoma de Ciudad Juárez (UACJ), calle José de Jesús Macías Delgado # 18100, 32579 Ciudad Juárez, Chihuahua, México.*
[c] *Departamento de Física, Universidad de Oviedo, 33007 Oviedo, Spain.*
[d] *Universidad Tecnológica de Tula-Tepeji, Av. Universidad Tecnológica No. 1000, C.P. 42830, El Carmen, Tula de Allende, Hidalgo, México.*

We have fabricated melt-spun ribbons of nominal composition ErMn$_2$ and studied their phase constitution and magnetocaloric (MC) properties by X-ray diffraction, scanning electron microscopy (SEM), magnetization and heat capacity measurements. The major phase formed shows the MgZn$_2$-type hexagonal structure (C14-type); however, both XRD and SEM analyses revealed the formation of impurity phases (*i.e.*, Er$_6$Mn$_{23}$ and ErMn$_{12}$). Ribbons exhibit a saturation magnetization of 149 Am^{2}kg^{-1} at 2 K and a Curie temperature of T_C = 15 K. A field-induced metamagnetic transition at very low critical magnetic fields was observed below 8 K that leads to a change of sign in the magnetic entropy change ΔS_M below this temperature (ΔS_M^{peak} = 2.5 Jkg^{-1}K^{-1} at 2 K and 5 T). For a magnetic field change of 5 T (2 T) applied along the ribbon length, the samples show a large peak value of the magnetic entropy change ΔS_M^{peak} of -20.5 (-10.8) Jkg^{-1}K^{-1}, a full-width at half-maximum δT_{FWHM} for the $\Delta S_M(T)$ curve of 20 (12) K, and a maximum adiabatic temperature change ΔT_{ad}^{max} of 7.4 (3.6) K. The obtained results are compared with the reported in literature by other authors for bulk alloys.

Keywords: ErMn$_2$ Laves phase; melt spun ribbons; magnetocaloric effect; magnetic entropy change; adiabatic temperature change.

---

* *Corresponding author.*
  Email address: jose.sanchez@ipicyt.edu.mx (J. L. Sánchez Llamazares)

1. INTRODUCTION

Magnetic refrigeration, an alternative cooling technology with a range of applications from room temperature to helium and hydrogen liquefaction temperatures [1], has boosted the interest in the magnetocaloric effect, characterized by the temperature and magnetic entropy changes occurring in the magnetic material when applying (or removing) an external magnetic field under adiabatic or isothermal conditions, respectively. Together with these properties, a key parameter for comparing MC materials is the refrigerant capacity (RC), which estimates the interchangeable heat between the refrigerant material and the reservoirs if an ideal refrigerant cycle is considered. This physical quantity is significant when the material shows sizeable maximum values of both the adiabatic temperature and magnetic entropy changes.

The MC properties of binary Laves phases based on rare-earths (R) have been extensively investigated due to their potential as magnetic refrigerants in the cryogenic temperature range [1-5]. Up to now, most studies have been focused mainly on RM_2 compounds with M = Al, Ni, and Co. However, recent work authored by Zuo *et al.* have reported a large reversible magnetic entropy change ΔS_M in RMn_2 compounds with several heavy R metals, such as Tb, Dy, Ho, and Er, underlying that they can be also considered promising working MC substances in the 10-80 K range [5]. It is important to note that the aximum adiabatic temperature change ΔT_{ad}^{max} for RMn_2 compounds has not been estimated yet. For bulk $ErMn_2$ alloys produced after a prolonged thermal annealing (1073 K; 7 days), they measured large values of the maximum magnetic entropy change ΔS_M^{peak} and RC (*i.e.*, -25.5 (-13.4) $Jkg^{-1}K^{-1}$ and 316 (100) Jkg^{-1}, respectively, for a magnetic field change $\mu_o\Delta H$ of 5 T (2 T); RC was estimated integrating the area below the full-width at half-maximum of the $\Delta S_M(T)$ curve). Present contribution focuses on this intermetallic alloy that crystallizes in the hexagonal $MgZn_2$-type structure of the Laves phases (C-14; space group P63/ mmc, number 194) [6,7]. In this compound, only Er atoms carry magnetic moment (*i.e.*, that of Mn is almost zero), which is close to that of free Er^{3+} ion (~ 8.8 versus 9 μ_B/f.u., respectively) [8,9]; Er^{3+} moments couple ferromagnetically through RKKY interaction below a Curie temperature T_C of 15 K [10]. Magnetization studies conducted on single crystals grown by Bridgman method show that the *c*-axis is the easy magnetization direction [9], and the saturation magnetization is reduced along the a and b axes; furthermore, if a magnetic field is applied along *a* and *b* axes, a critical magnetic field of ~ 1.2 T induces a metamagnetic transition that reorients the magnetic moments in a canted magnetic structure in which they tilt alternatively ±30º from the a (*b*) axis in the *a-c* (*b-c*) plane [9]. In a more recent study, carried out on single crystal grown by Czochralski method [10], is reported that the critical field that induces the transition along the *a*-axis is reduced to 0.7 T.

Rapid solidification by melt spinning technique has been effectively applied in the last few years to produce different crystalline R-based MC materials, such as $LaFe_{13-x}Si_x$ [11], $Gd_5(SiGeSn)_4$ [12], RNi_2 (R = Tb, Dy) [13-15], $NdPrFe_{17}$ [16], Dy_3Co [17], and DyNi [18]. In most of the cases, a single phase is formed in the as-solidified alloy ribbons, or after a much shortened annealing compared to their bulk counterparts. The aim of the present investigation has been to study the MC behavior of $ErMn_2$ melt-spun ribbons. Their MC properties were determined from both magnetization and heat capacity measurements; the results are compared with those obtained for bulk samples.

2. EXPERIMENTAL PROCEDURES

Ribbon flake samples were fabricated from a bulk Ar arc melted pellet of nominal composition $ErMn_2$; highly pure Er (99.9 %, Sigma-Aldrich) and Mn (99.998 %, Alfa Aesar) were used as raw materials. Samples were melted three times to ensure an adequate starting homogeneity; special care was taken to keep the 1:2 composition in the starting master alloys. Rapid solidification process was carried under UHP Ar atmosphere using an Edmund Bühler SC melt spinner system; once molten, the alloy was ejected onto the polished surface of a copper wheel rotating at a surface linear speed of 15 ms^{-1}.

X-ray diffraction (XRD) patterns of finely powdered samples were collected with a Rigaku smartlab high-resolution diffractometer using Cu-K_α radiation ($\lambda = 1.5418$ Å); the ribbons were grounded using an agate mortar. The scan was carried out in the interval $15^o \leq 2\theta \leq 100^o$ with 0.01^o of step increment. Microstructure was studied with a dual beam Helios Nanolab, ESEM FEI Quanta 200 equipped with an energy dispersive spectroscopy (EDS) system.

Magnetic measurements were performed by vibrating sample magnetometry in a Quantum Design PPMS® Dynacool®-9T system; the typical size of the measured sample was 3.5 mm in length and 0.6 mm in width. The magnetic field μ_oH was applied along the ribbon axis (*i.e.*, the direction of ribbon formation or longitudinal direction) to minimize the effect of the internal demagnetizing field. The low-field (5 mT) magnetization as a function of temperature curve $M(T)$ was measured between 2 and 100 K under zero-field-cooled (ZFC) and field-cooled (FC) regimens, respectively, where $M_{FC}(T)$ curve was used to estimate the T_C value while the high-field $M(T)$ curve was measured on heating (FH) under $\mu_oH = 5$ T; all $M(T)$ curves were measured with a temperature sweeping rate of 1.0 $Kmin^{-1}$. Heat capacity (HC) as a function of temperature was measured by means of the relaxation method using the HC option of a Quantum Design PPMS® Evercool®-9T system. Measurements were performed using the vertical HC puck. Thus, as for magnetization measurements, the magnetic field was applied along

the ribbon major length. $\Delta S_M(T)$ curves were obtained from: (i) numerical integration of the Maxwell relation, *i.e.,* $\Delta S_M(T, \mu_o H) = \mu_o \int_0^{\mu_o H_{max}} \left[\frac{\partial M(T, \mu_o H')}{\partial T} \right]_{\mu_o H'} dH'$; (ii) total entropy change $S_T(T)$ curves obtained from the specific heat $c_p(T, \mu_o H)$ curves measured at 0, 2 and 5 T. The adiabatic temperature change as a function of temperature and applied magnetic field change $\Delta T_{ad}(T, \mu_o \Delta H)$ curves were indirectly obtained from the total $S_T(T, \mu_o H)$ curves.

3. RESULTS AND DISCUSSION

The indexed room temperature XRD pattern of the as-quenched ribbons is depicted in Figure 1(a). Its Le Bail profile fitting was done using the FullProf Suite package [19]. The Bragg reflections of the major phase performed correspond to a hexagonal $MgZn_2$-type crystal structure of the Laves phases (C-14; space group P63/mmc, number 194), with lattice parameters $a = b = 0.52989(1)$ nm and $c = 0.86516(2)$ nm, which are in good agreement with the reported for bulk alloys [5, 10, 20]. The additional minor intensity XRD peaks of the experimental pattern belong to 6:23 and 1:12 phases. Both are stable phases of the binary Er-Mn phase diagram [21]. It must be noticed that the peaks appearing in the pattern show a noticeable broadening; this suggest that the rapid solidification process alters the local structural equilibrium order. Figure 1(b) shows typical SEM micrographs at different magnifications of the ribbon's fracture microstructure. While their thickness is around 30 µm, the major phase crystallizes into micronic in size grains with no preferred orientation with respect to both ribbon surfaces. It is worth noting that, in agreement with XRD analysis, the SEM micrographs show the precipitation of small bright particles along grain boundaries of the major phase confirming the presence of secondary phases.

Figure 2 shows the temperature dependence of the magnetization, $M(T)$, measured under applied magnetic fields of 5 mT following ZFC and FC protocols (open and full red circles, respectively) and 5 T (black open circles). The former indicates that the major phase formed in ribbons is the ferromagnetic $ErMn_2$ compound with a Curie temperature $T_C = 15 \pm 1$ K (value estimated from the minimum of the dM^{FC}/dT versus T curve shown at the inset), which coincides with the ferromagnetic transition temperature previously reported for this binary compound in bulk alloys [5, 9, 20]. However, the saturation magnetization, $M_S = 149 \pm 1$ A m^2 kg^{-1} at $T = 2$ K and 5 T (equivalent to ~ 7.4 μ_B/f.u.), is reduced with respect to the reported for the bulk alloys [9]; such decrease is attributed to the local disorder and the presence of spurious 6:23 and 1:12 phases, which show a complex non-collinear [22] and antiferromagnetic [23] magnetic ordering, respectively. Considering the absence of hints of other

4

magnetic phase transition in the $M(T)$ curves than that of the majority phase, we can conclude that the net contribution of these impurity phases to the total magnetic moment of the alloy is negligible, at least for magnetic fields up to 5T.

Figure 3(a) shows the set of isothermal magnetization curves $M(\mu_oH)$ collected every 2 K from 2 K to 60 K up to a maximum applied magnetic field of 5 T across the ferromagnetic to paramagnetic transition. At each temperature, the magnetization was measured for a large number of selected magnetic field values to improve the accuracy of the ΔS_M calculation from Maxwell relation. Figure 3(b) shows the resulting $\Delta S_M(T)$ curves for $\mu_o\Delta H = 2$ and 5 T. Apart from the large absolute maximum values, it must be noticed the change of sign of ΔS_M at 2 T below 8 K; this behavior is ascribed to the field-induced metamagnetic transition along the a-axis. The low-field region of the isothermal magnetization curves is presented in Figure 4; the change in the slope of the curve at 2 K appears at a critical field roughly estimated as 0.12 T, this is in contrast with respect to the observed in single crystals where much higher critical fields field have been reported [9,10]. The convex curvature around the origin of the Arrott´s plots between 2 and 10 K, displayed at the inset of Figure 3(b), stresses the first-order character of this metamagnetic transition.

Figure 5(a) shows the thermal dependence of specific heat as well as the total entropy change at 0, 2 and 5 T. The zero-field $c_p(T,\mu_oH)$ curve shows the characteristic λ–type peak of second-order phase transition, that in agreement with magnetization measurements, is located at 15 K; the measured c_p values are consistent with those previously reported by Okamoto et al. [24]. With increasing temperature, the peak shifts toward higher temperatures and becomes broader. The $\Delta S_M(T)$ curves at 2 and 5 T obtained from the $\Delta S_T(T)$ dependencies that are plotted in the inset of Figure 5(a), are shown in Figure 5(b). As expected, the maximum entropy change occurs at the temperature at which $c_p(T,0) = c_p(T, \mu_oH)$ and $\frac{\partial c_p(T,\mu_oH)}{\partial T} < \frac{\partial c_p(T,0)}{\partial T}$ [25]. At the inset, we compare the $\Delta S_M(T)$ curves obtained from the Maxwell relation and heat capacity measurements. The excellent agreement found between both approaches highlights the accuracy and reliability of the experimental procedure followed to obtain the primary experimental data to estimate the MC effect curves from both methods. A key point in this sense is the minimization of the internal demagnetization field for the determination of experimental data from both methods as has been emphasized in Ref. 42; another important point was the strict control of criteria for evaluating the quality of heat capacity data. Figure 5(b) also shows the $\Delta T_{ad}(T)$ dependence (estimated from the $S_T(T,\mu_oH)$ curves). Tables 1 and 2 compare the magnetocaloric data obtained for the as-solidified melt-spun fabricated with those reported in Ref. [5] for bulk alloys and

$\left|\Delta T_{ad}^{max}\right|$ contrasted with the stated in literature with other MC materials with magnetic phase transition close to 20 K. Whereas $\left|\Delta T_{ad}^{max}\right|$ is similar to those reported for other Laves phases, such as $ErCo_2$, $DyNi_2$, and $HoAl_2$, the reduced magnetization jump ΔM leads to inferior (~ 20 %) $\left|\Delta S_M^{peak}\right|$ compared with the bulk $ErMn_2$ alloy. Note however that the ΔS_M peak in ribbons spreads out over a larger (about 20 %) temperature interval, which has to main consequences: (i) the maximum working temperature range expands, being the cold reservoir at 12 K (11 K) and hot reservoir at 30 K (28 K) under a magnetic field change of 5 T (2 T); and (ii) it neutralizes the effect of the reduction of the magnetic entropy change on the refrigerant capacity (see Table 1).

4. CONCLUSIONS

The hexagonal $MgZn_2$-type crystal structure of the Laves phase (C14) crystallizes as major phase in as-solidified $ErMn_2$ melt-spun ribbons coexisting with small intergranular precipitates identified as Er_6Mn_{23} and $ErMn_{12}$; this is in rough agreement with the reported for bulk alloys fabricated by conventional arc melting followed by a long-term high-temperature thermal annealing. The temperature dependencies of the magnetic entropy change determined from isothermal magnetization and isofield heat capacity measurements are in excellent agreement. While $\Delta S_M(T)$ curves show a $\left|\Delta S_M^{peak}\right|$ around 20 % less than the reported for bulk alloys, its becomes broader showing an extended full-width at half-maximum nearby a 20 %, which is beneficial for refrigerant applications. Together with this, the maximum adiabatic temperature change values determined are comparable to the reported for most of R-based alloys with a first- or second order transition below 40 K referred as promising magnetic refrigerants at cryogenic temperatures. In conclusion, we have demonstrated that the fabrication of $ErMn_2$ alloys by melt spinning is a feasible route to obtain materials that guaranties fast heat exchange, thanks to its large surface to volume ratio, but maintaining the magnetocaloric properties.

REFERENCES

[1] K.A. Gschneidner Jr., K. Pecharsky, A.O. Tsokol, Rep. Prog. Phys. **68** (2005) 1479.

[2] N.A. de Oliveira, P.J. von Ranke, Rep. Prog. Rep. **489** (2010) 89.

[3] N.H. Duc, D.T. Kim Anh, J. Magn. Magn. Mater. **242-245** (2002) 873.

[4] Niraj K. Singh, K.G. Suresh, A.K. Nigam, S.K. Malik, A.A. Coelho, S. Gama, J. Magn. Magn. Mater. **317** (2007) 68.

[5] Wenliang Zuo, Fengxia Hu, Jirong Sun, Baogen Shen, J. Alloys Compd. **575** (2013) 162.

[6] J.H. Wernick, S.E. Haszko, J. Phys. Chem. Solids **18** (1961) 207.

[7] H.R. Kirchmayr, A. Angew. Phys. **27** (1969) 18.

[8] G.P. Felcher, L.M. Corliss, J.M. Hastings, J. Appl. Phys. **36** (1965) 1001.

[9] Y. Makihara, Y. Andoh, Y. Hashimoto, H. Fujii, T. Okamoto, J. Phys. Soc. Jpn. **52** (1983) 629.

[10] E. Talik, M. Kulpa, T. Mydlarz, J. Kusz, H. Böhm, J. Alloys Compd. **348** (2003) 12.

[11] A. Yan, K.-H. Müller, L. Schultz, O. Gutfleisch, J. Appl. Phys. **99** (2006) 08K903.

[12] T. Zhang, Y. Chen, Y. Tang, J. Phys. D: Appl. Phys. **40** (2007) 5778.

[13] J.L. Sánchez Llamazares, C.F. Sánchez-Valdés, P.J. Ibarra-Gaytán, P. Álvarez-Alonso, P. Gorria, J.A. Blanco, J. Appl. Phys. **113** (2013) 17A912.

[14] P.J. Ibarra-Gaytán, J.L. Sánchez Llamazares, Pablo Álvarez-Alonso, C.F. Sánchez-Valdés, Pedro Gorria, J.A. Blanco, J. Appl. Phys. **117** (2015) 17C116.

[15] P.J. Ibarra-Gaytan, C.F. Sánchez-Valdés, J.L. Sánchez Llamazares, P. Álvarez-Alonso, P. Gorria, J.A. Blanco, Appl. Phys. Lett. **103** (2013) 152401.

[16] C.F. Sánchez-Valdes, P.J. Ibarra-Gaytán, J.L. Sánchez Llamazares, M. Avalos-Borja, Pablo Álvarez-Alonso, P. Gorria, J.A. Blanco, Appl. Phys. Lett. **104** (2014) 212401.

[17] J.L. Sánchez Llamazares, H. Flores-Zúñiga, Pablo Álvarez-Alonso, C.F. Sánchez-Valdés, G.A. Lara Rodríguez, M.L. Fernández-Gubieda, J. Appl. Phys. **117** (2015) 17A706.

[18] R. Rajivgandhi, J. Arout Chelvane, A.K. Nigam, Je-Geun Park, S.K. Malik, R. Nirmala, J. Magn. Magn. Mater. **418** (2016) 9.

[19] J. Rodríguez-Carvajal, Physica B **192** (1993) 55.

[20] K. Inoue, Y. Nakamura, A.V. Tsvyashchenko, L. Fomicheva, J. Phys. Soc. Jpn. **64** (1995) 2175.

[21] X.J. Liu, Y. Lu, M.H. Chen, D.L. Zhao, C.P. Wang, K. Ishida, J. Phase Equilib. Diff. **35** (2014) 612.

[22] B. Ouladdiaf, J. Deportes, J. Rodríguez-Carvajal, Physica B **213-214** (1995) 330.

[23] J. Deportes, D. Givord, R. Lemaire, H. Nagai, Physica B **86-88B** (1977) 69.

[24] T. Okamoto, H. Nagata, H. Fujii, Y. Makihara, J. Magn. Magn. Mater. **70** (1987) 139.

[25] V. Pecharsky, K. Gschneidner, A. Pecharsky, A. Tishin, Phys. Rev. B **64** (2001) 144406

[26] P.J. von Ranke, V.K. Pecharsky, K.A. Gschneidner, Jr., Phys. Rev. B **58** (1998) 12110.

[27] T. Hashimoto, K. Matsumoto, T. Kurihara, T. Numazawa, A. Tomokiyo, H. Yayama, T. Goto, S. Todo, M. Sahashi, Adv. Cryog. Eng. **32** (1986) 279.

[28] P.J. von Ranke, E.P. Nóbrega, I.G. de Oliveira, A.M. Gomes, R.S. Sarthour, Phys. Rev. B **63** (2001) 184406.

[29] A.M. Tishin, V.K. Pecharsky, A.O. Pecharsky, K.A. Gschneidner Jr., (2002) unpublished results.

[30] A.M. Tishin and Y.I. Spichkin, *The magnetocaloric effect and its applications* (IOP, Bristol, 2003).

[31] M.I. Ilyn, A.M. Tishin, V.K. Pecharsky, A.O. Pecharsky, K.A. Gschneidner Jr, CEC/ICMC (2001).

[32] J.L. Wang, S.J. Campbell, J.M. Cadogan, A.J. Studer, R. Zeng, S.X. Dou, Appl. Phys. Lett. **98** (2011) 232509.

[33] T. Samanta, I. Das, S. Banerjee, Appl. Phys. Lett. **91** (2007) 152506.

[34] L.W. Li, D.X. Huo, H. Igawa, K. Nishimura, J. Alloys Comp. **509** (2011) 1796.

[35] L.W. Li, H. Igawa, K. Nishimura, D.X. Huo. J. Appl. Phys. **109** (2011) 083901.

[36] K.A. Gschneidner Jr., V.K. Pecharsky, Annu. Rev. Mater. Sci. **30** (2000) 387.

[37] L. Li, K. Nishimura, H. Yamane, Appl. Phys. Lett. **94** (2009) 102509.

[38] L. Li, K. Nishimura, J. Phys. D: Appl. Phys. **42** (2009) 145003.

[39] R. Rawat, I. Das, J. Phys.: Condens. Matter **13** (2001) L57.

[40] A.O. Pecharsky, Yu Mozharivskyj, K.W. Dennis, K.A. Gschneidner Jr., R.W. McCallum, G.J. Miller, V.K. Pecharsky, Phys. Rev. B **68** (2003) 134452.

[41] L. Li, K. Nishimura, J. Appl. Phys. **106** (2009) 023903.

[42] B. Schwarz, N. Mattern, J.D. Moore, K.P. Skokov, O. Gutfleisch, J. Eckert, J. Magn. Magn. Mater. **323** (2011) 1782.

FIGURE CAPTIONS

FIG. 1. (a) Le Bail profile fitting of the XRD pattern of as-solidified $ErMn_2$ ribbons (CuK_α). The major phase shows the $MgZn_2$-type hexagonal structure of the Laves phases (C14; $a = b = 0.52989(1)$ nm; $c = 0.86516(2)$ nm); the diffraction lines of 6:23 and 1:12 phases are also present. (b) SEM micrographs of the cross-section and typical microstructure shown by as-solidified $ErMn_2$ melt-spun ribbons.

FIG. 2. $M(T)$ curves measured at 5 mT following ZFC and FC regimens (open and full red symbols, respectively), and 5 T (open black symbols; FH). Inset: $dM/dT(T)$ curve at 5 mT for the FC $M(T)$ curve; $T_C = 15 \pm 1$ K.

FIG. 3. (a) $M(\mu_oH)$ curves measured up to 5 T for as-solidified $ErMn_2$ ribbon. $M_S^{2K} = 149 \pm 1$ Am^2kg^{-1}. (b) $\Delta S_M(T)$ curves at $\mu_o\Delta H = 2$ and 5 T. Inset: Arrott plots between 2 and 28 K.

FIG. 4. Low-field region of the isothermal magnetization curves measured for $ErMn_2$ melt-spun ribbons.

FIG. 5. (a) Specific heat as a function of temperature measured at 0, 2 and 5 T. Inset: $S_T(T)$ curves at 0, 2 and 5 T. (b) $\Delta S_M(T)$ and $\Delta T_{ad}(T)$ curves at $\mu_o\Delta H = 2$ and 5 T. Inset: comparison of the $\Delta S_M(T)$ curves obtained from magnetization and specific heat measurements at $\mu_o\Delta H = 2$ and 5 T.

TABLE CAPTION

TABLE 1. Magnetocaloric properties of as-solidified $ErMn_2$ melt-spun ribbons determined from heat capacity and isothermal magnetization measurements. For the sake of comparison, the data reported in ref. 5 is included.

TABLE 2. ΔT_{ad}^{max} at 2 and 5 T for $ErMn_2$ melt-spun ribbons compared with the available data reported for other RM_2 Laves phases (M = Al, Ni, Co) and other materials with a transition temperature below 40 K.

TABLE 1. Magnetocaloric properties of as-solidified $ErMn_2$ melt-spun ribbons determined from heat capacity and isothermal magnetization measurements. For the sake of comparison, the data reported in Ref. 5 is included.

	$ErMn_2$ melt-spun ribbons				$ErMn_2$ bulk alloy [**]	
method	$c_p(T,\mu_oH)$		$M(\mu_oH)$		$M(\mu_oH)$	
$\mu_o\Delta H$ (T)	**2**	**5**	**2**	**5**	**2**	**5**
$|\Delta S_M^{peak}|$ (Jkg^{-1}K^{-1})	10.8	20.5	10.8	20.4	13.4	25.4
T_{ad}^{max} (K)	3.6	7.4	-	-	-	-
RC-1* (Jkg^{-1})	134	409	135	405	135 [*]	418 [*]
RC-2 (Jkg^{-1})	104	314	106	315	100	316
δT_{FWHM} (K)	12	20	13	20	10	16.4
T_{hot} (K)	24	31	24	30	11.7 [*]	12 [*]
T_{cold} (K)	12	11	11	10	21.7 [*]	28.5 [*]
RC-3 (Jkg^{-1})	67	206	68	206	-	-
δT^{RC-3} (K)	13	23	13	22	-	-
T_{hot}^{RC-3} (K)	25	34	24	32	-	-
T_{cold}^{RC-3} (K)	12	11	11	10	-	-

[*] Estimated from the $\Delta S_M(T)$ curve reported.
[**] Ref. 5 [W. Zuo et al., JALCOM **575**, 162 (2013)].

TABLE 2. $\Delta T_{\mathrm{ad}}^{\mathrm{max}}$ at 2 and 5 T for ErMn$_2$ melt-spun ribbons compared with the available data reported for other RM$_2$ Laves phases (M = Al, Ni, Co) and other materials with a transition temperature below 40 K.

Alloy	T_{C} (K)	$\Delta T_{\mathrm{ad}}^{\mathrm{max}}$ (K) 2 T	5 T	Reference
ErMn$_2$ ribbons [*]	15	3.6	7.4	this work
ErAl$_2$	11.7	-	9	26, 27
ErNi$_2$	6.6	-	8	28
ErCo$_2$	35	3.2	7.2	29
HoNi$_2$	13	-	13.8	28
DyNi$_2$	21	4	8.5	26
(Dy$_{0.25}$Er$_{0.75}$)Al$_2$	24	-	8.5	30
HoAl$_2$	31	4.6	-	31
TbNi$_2$	37	-	8.1	28
NdMn$_2$Ge$_{0.4}$Si$_{1.6}$	36	2.1	-	32
ErRu$_2$Si$_2$	5.5	-	12.9	33
TbCo$_3$B$_2$	30	4	7.3	34
DyCo$_3$B$_2$	22	6.4	-	35
Gd$_5$Si$_{0.15}$Ge$_{3.85}$	40	-	8.8	36
GdCo$_2$B$_2$	25	6.7	15.4	37
NdCo$_2$B$_2$	27	3.3	5.8	38
GdPd$_2$Si	17	3.2	8.6	39
PrNi	20	0.8	1.7	40
PrCo$_2$B$_2$	16	4.3	8.1	41

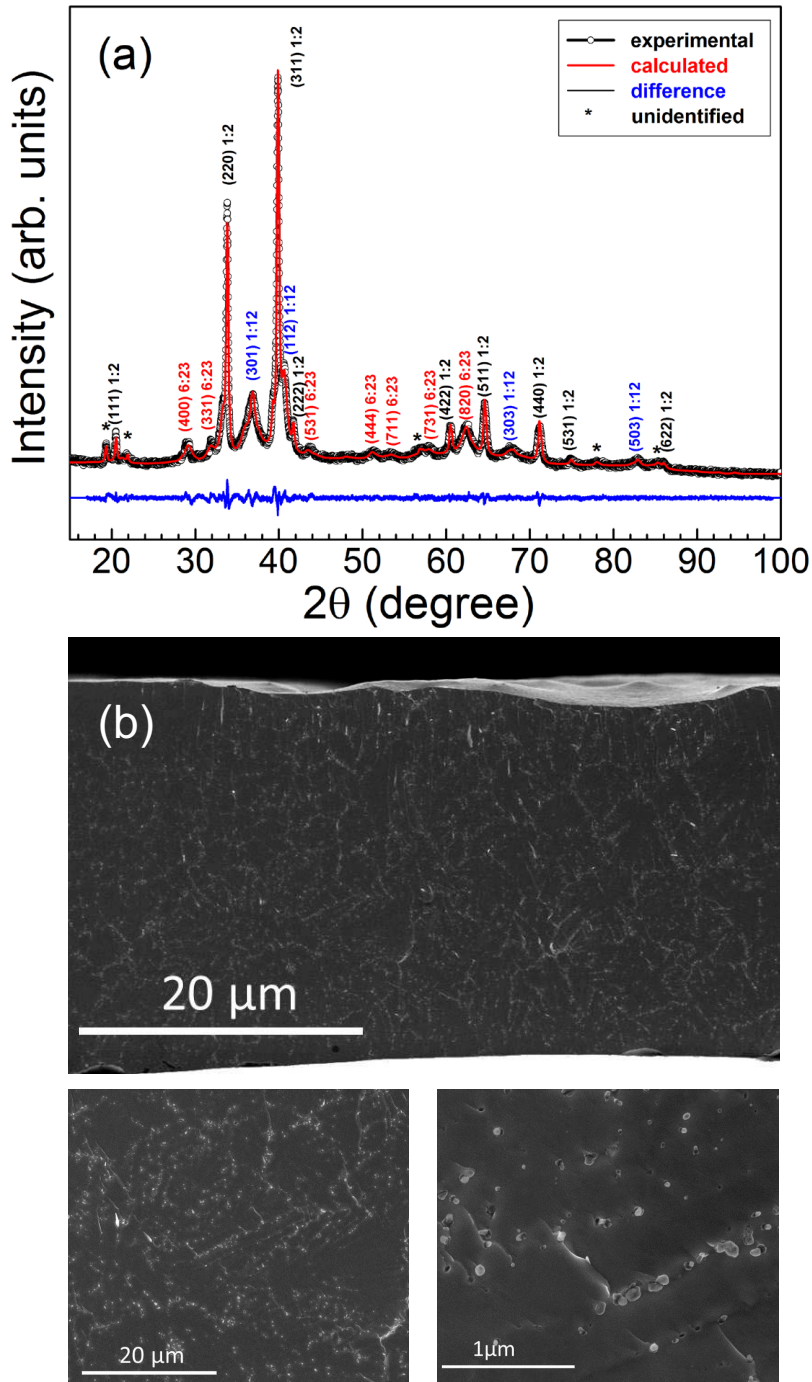[*] No $\Delta T_{\mathrm{ad}}^{\mathrm{max}}$ data reported for bulk alloys.

FIG. 1. (a) Le Bail profile fitting of the XRD pattern of as-solidified $ErMn_2$ ribbons (CuK_α). The major phase shows the $MgZn_2$-type hexagonal structure of the Laves phases (C14; $a = b = 0.52989(1)$ nm; $c = 0.86516(2)$ nm); the diffraction lines of 6:23 and 1:12 phases are also present. (b) SEM micrographs of the cross-section and typical microstructure shown by as-solidified $ErMn_2$ melt-spun ribbons.
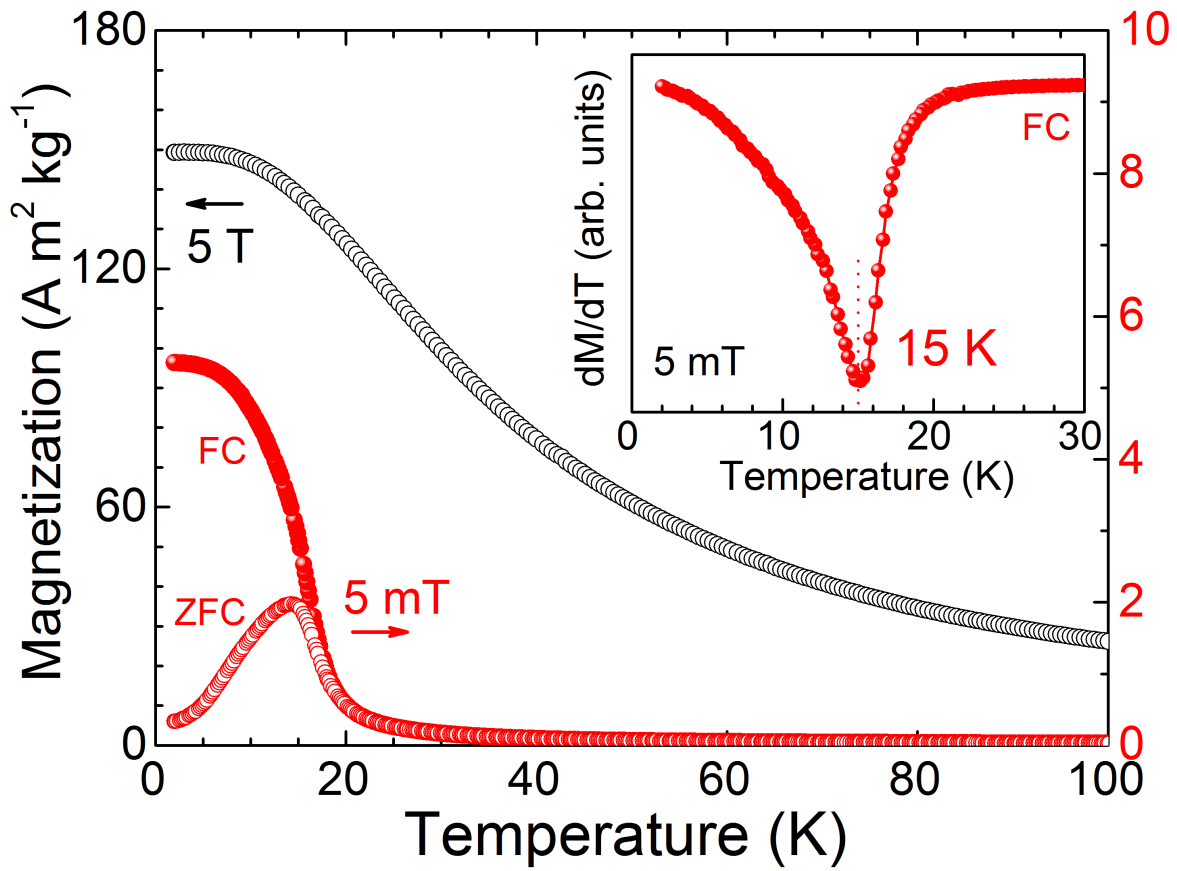
FIG. 2. $M(T)$ curves measured at 5 mT following ZFC and FC regimens (open and full red symbols, respectively), and 5 T (open black symbols; FH). Inset: $dM/dT(T)$ curve at 5 mT for the FC $M(T)$ curve; $T_C = 15 \pm 1$ K.
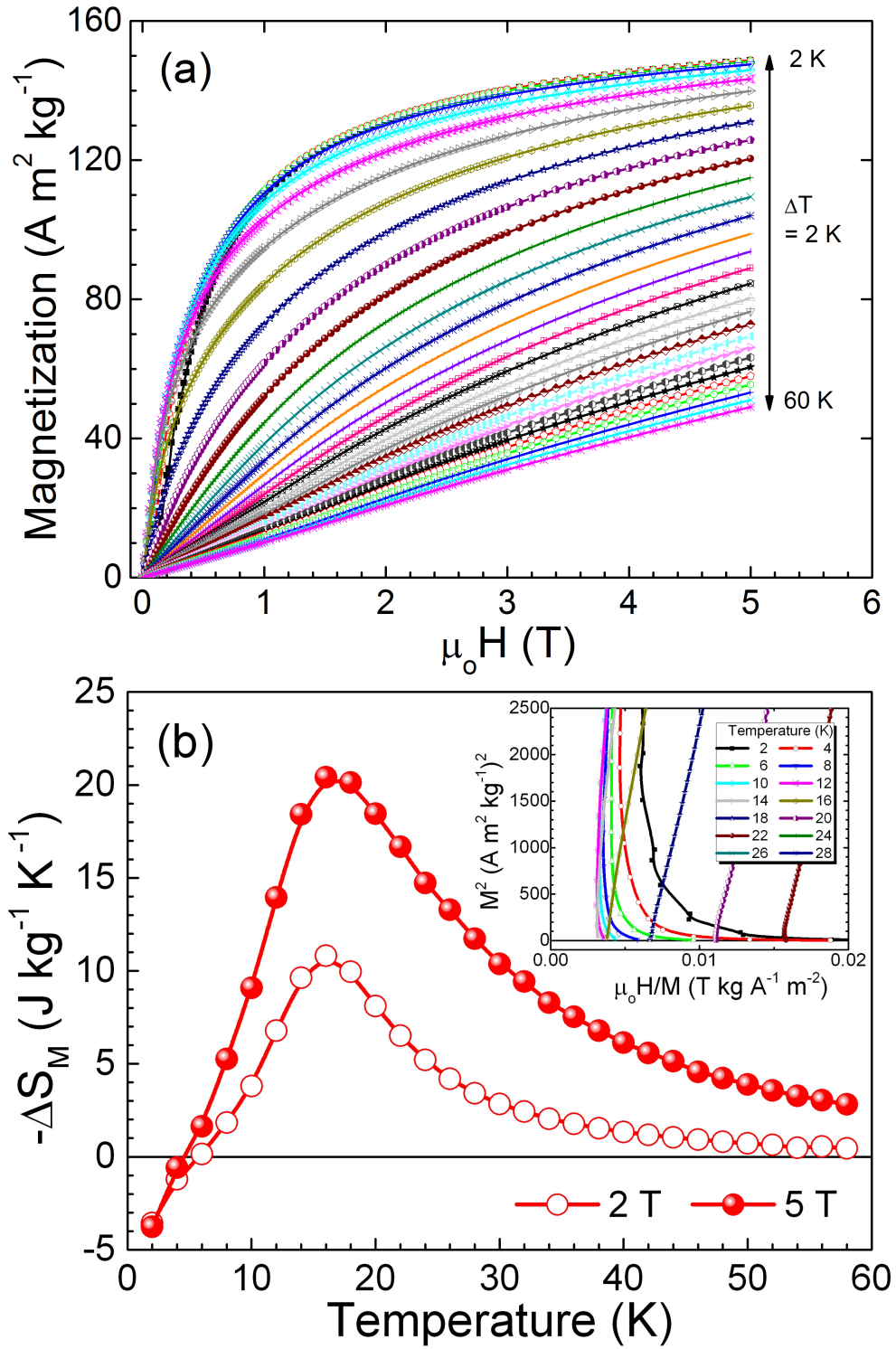
FIG. 3. (a) $M(\mu_o H)$ curves measured up to 5 T for as-solidified ErMn$_2$ ribbon. $M_S^{2K} = 149 \pm 1$ Am^{2}kg^{-1}. (b) $\Delta S_M(T)$ curves at $\mu_o \Delta H = 2$ and 5 T. Inset: Arrott plots between 2 and 28 K.
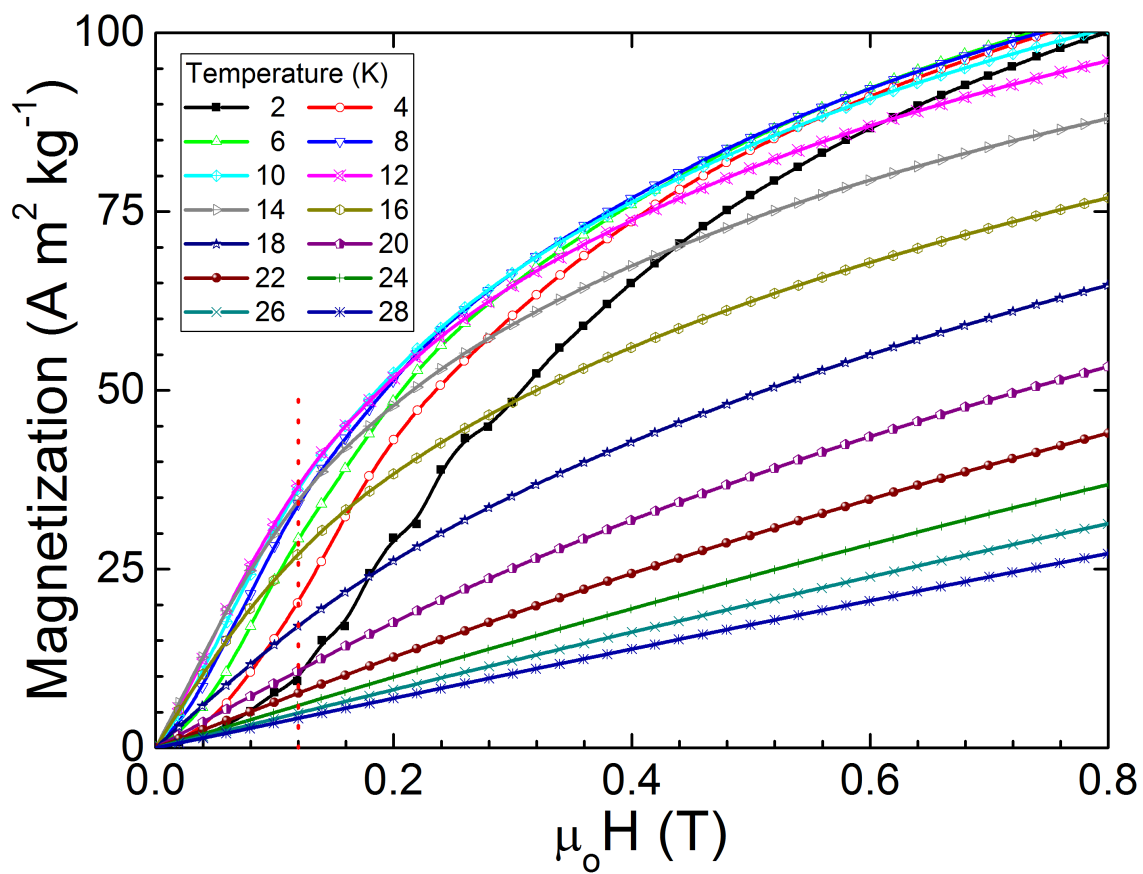
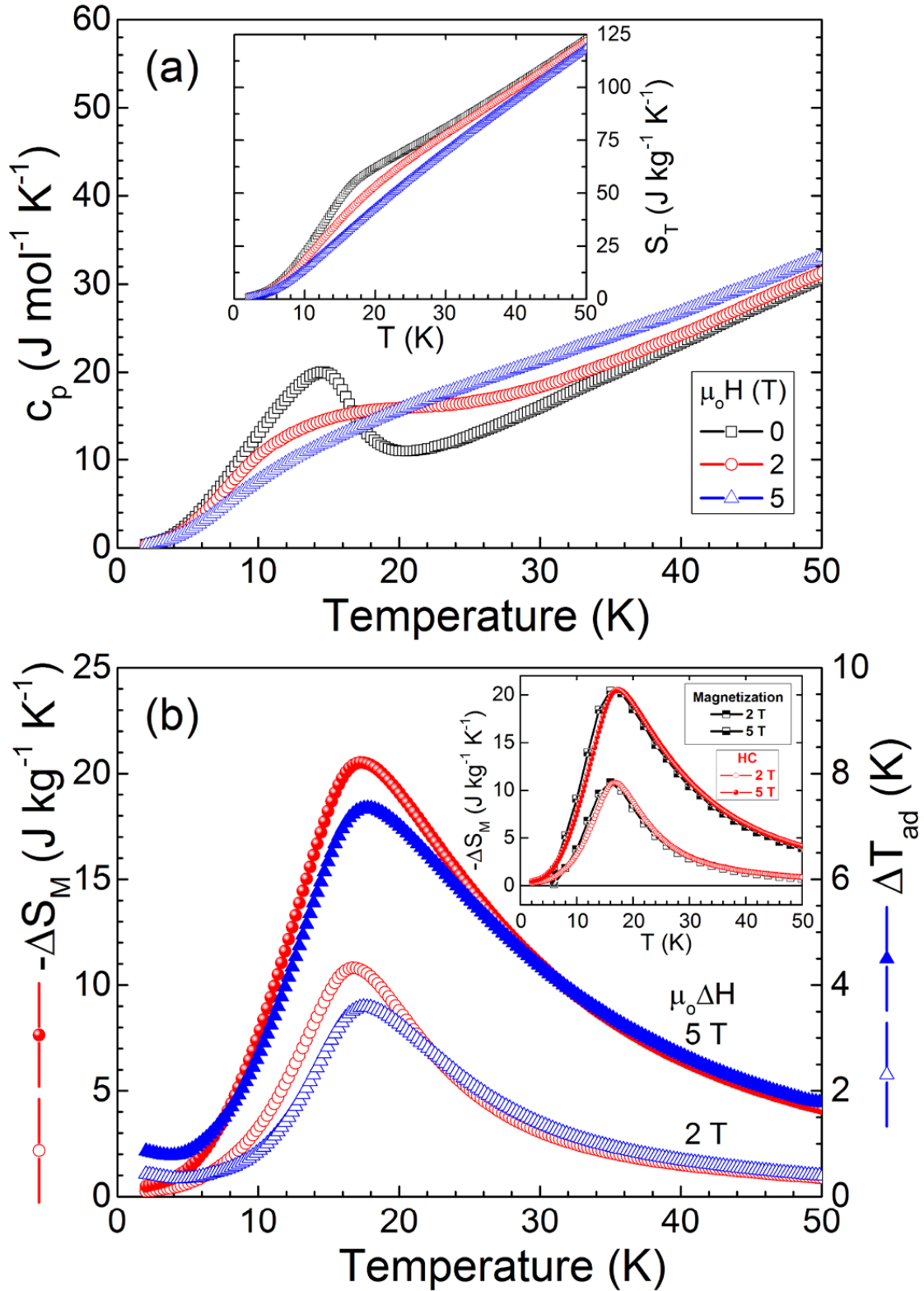**FIG. 4.** Low-field region of the isothermal magnetization curves measured for ErMn₂ melt-spun ribbons.

FIG. 5. (a) Specific heat as a function of temperature measured at 0, 2 and 5 T. Inset: $S_T(T)$ curves at 0, 2 and 5 T. (b) $-\Delta S_M(T)$ and $\Delta T_{ad}(T)$ curves at $\mu_o \Delta H$ = 2 and 5 T. Inset: comparison of the $-\Delta S_M(T)$ curves obtained from magnetization and specific heat measurements at $\mu_o \Delta H$ = 2 and 5 T.

16